Lennard-Jones fluids in cylindrical pores: Nonlocal theory and computer simulation

Brian K. Peterson, Keith E. Gubbins, Grant S. Heffelfinger, Umberto Marini Bettolo Marconi,[a] and Frank van Swol
School of Chemical Engineering, Cornell University, Ithaca, New York 14853

(Received 15 January 1988; accepted 5 February 1988)

We present adsorption isotherms, phase diagrams, and density profiles for a Lennard-Jones fluid confined to a cylindrical pore. In particular, we concentrate on the gas–liquid transition in the pore (capillary condensation). We compare simulations for a series of radii and different temperatures with mean field density functional theory (MFT). Two forms of MFT are considered, the simple local density approximation (LDA) and Tarazona's nonlocal or smoothed density approximation (SDA). We find that the SDA provides a quite accurate description of fluid structure in the pore and that it produces phase diagrams in good agreement with the simulation data. For larger radii and temperatures $T/T_c \gtrsim 0.6$ the SDA shows steep rises in adsorption close to the transition. This strongly affects the shape of the coexistence curve in the T, $\bar{\rho}$ plane. Here $\bar{\rho}$ is defined as the average density inside the pore. This behavior is confirmed by the simulation. In contrast, LDA gives a poor representation of the fluid structure and this underlies the failure to reproduce the phase diagrams and adsorption isotherms found with SDA or simulation. For extremely small radii ($R^* \approx 1$) the simulation adsorption isotherms are smooth, and for not too low a temperature they are accurately described by an approach which starts from the potential distribution theorem and uses perturbation theory for the true one-dimensional fluid.

I. INTRODUCTION

Over the past three or four years there has been renewed interest in understanding the behavior of simple fluids in narrow pores. This interest has focused on the density profile and adsorption inside the pore, phase transitions and hysteresis effects, and wetting and prewetting phenomena. Most of the initial studies were based on the local form of the density functional theory,[1–10] although some workers[11–13] have used integral equation theory as a starting point. Computer simulations[4,8,11–23] have also played an important role, both in elucidating the phenomena themselves and in testing theories.

In the local density functional theory used in most of the work so far, the contributions of the repulsive intermolecular forces to the free energy density at some point $\mathbf{r}$ in the fluid is approximated by that of a hard sphere fluid of *uniform* density $\rho(\mathbf{r})$, where $\rho(\mathbf{r})$ is the density of the nonuniform fluid in the pore locally at $\mathbf{r}$. This approximation is known to give very poor results for the density profile, particularly near the walls where the density variation is very large (see, e.g., Refs. 17 and 19). Moreover, this defect in the local theory leads to errors in the predicted phase transitions and hysteresis loops, especially for small pores.[19] In nonlocal theories the repulsive part of the free energy density is usually approximated by that for a uniform hard sphere fluid at some "smoothed" density $\tilde{\rho}(\mathbf{r})$, rather than at the local density $\rho(\mathbf{r})$. This smoothed or "coarse-grained" density incorporates in some way the density fluctuations in the vicinity of $\mathbf{r}$. Usually, $\tilde{\rho}(\mathbf{r})$ is chosen so that the theory gives good results for the direct correlation function $c(r)$, and hence also for the thermodynamic properties, of the uniform hard sphere fluid. Several variations on this approach have been proposed. We have chosen to use a version due to Tarazona,[9,24] since we believe it best combines the desirable features of nonlocal theory with computational tractability. Other versions of nonlocal theory have been proposed, e.g., Refs. 25, 26, and 23 but these theories demand much greater computational effort.

We report nonlocal theory calculations of the density profile, adsorption, hysteresis effects, and phase transitions for a Lennard-Jones (LJ) fluid in straight cylindrical pores with structureless walls. We also report new computer simulation results using both the grand canonical Monte Carlo (GCMC) and molecular dynamics (MD) methods. The nonlocal theory is tested using these and previous simulation results, and is also compared to the simpler local theory. We describe the theoretical and simulation methods in Secs. II and III, respectively. The results are given in Sec. IV.

II. THEORY

In this section we describe the density functional theory that we applied in our study of capillary condensation in cylindrical pores. We follow rather closely the presentation given by Tarazona *et al.*,[9] to which we refer the reader for more details and results for wetting at a single wall and capillary condensation in a slit geometry. Our starting point is the grand potential functional,[27] which is the appropriate functional of the density profile $\rho(\mathbf{r})$ when one considers a fluid in an external field $V_{\text{ext}}(\mathbf{r})$ at a fixed temperature T and chemical potential μ

$$\Omega[\rho(\mathbf{r})] = \mathcal{F}[\rho(\mathbf{r})] + \int d\mathbf{r}\, \rho(\mathbf{r})[V_{\text{ext}}(\mathbf{r}) - \mu]. \quad (1)$$

[a] Present address: Dipartimento di Fisica, II Universita di Roma "Tor Vergata", Rome, Italy.

Downloaded 09 Mar 2007 to 141.108.2.9. Redistribution subject to AIP license or copyright, see http://jcp.aip.org/jcp/copyright.jsp

Here $\mathscr{F}[\rho(\mathbf{r})]$ denotes the Helmholtz free energy functional. At thermodynamic equilibrium $\Omega[\rho(\mathbf{r})]$ is a global minimum with respect to variations in $\rho(\mathbf{r})$, and at this minimum its value is equal to the thermodynamic grand potential Ω. The key step in density functional theory is to specify an approximate form for $\Omega[\rho(\mathbf{r})]$ that is both tractable and accurate. To this end one usually[27] divides $\mathscr{F}[\rho(\mathbf{r})]$ into a repulsive and an attractive contribution. The repulsive part is subsequently represented by a hard sphere contribution, while the attractive contribution is treated in a mean-field fashion,

$$\mathscr{F}[\rho(\mathbf{r})] = \mathscr{F}_{\rm hs}[\rho(\mathbf{r})] + \frac{1}{2}\int d\mathbf{r}\int d\mathbf{r}'\,\rho(\mathbf{r})\rho(\mathbf{r}')\Phi_a(|\mathbf{r}-\mathbf{r}'|). \tag{2}$$

Here, Φ_a denotes the attractive part of the fluid pair potential. The hard sphere functional $\mathscr{F}_{\rm hs}[\rho(\mathbf{r})]$ is unknown and one proceeds by making further approximations, two of which we will discuss below.

A. Local density approximation (LDA)

In this approximation, that was first used by Sullivan,[28] one writes

$$\mathscr{F}_{\rm hs}[\rho(\mathbf{r})] = \int d\mathbf{r}\, f_{\rm hs}(\rho(\mathbf{r})), \tag{3}$$

where $f_{\rm hs}(\rho(\mathbf{r}))$ is the hard sphere free energy density of a uniform fluid with density equal to the local density at $\mathbf{r}$. As mentioned above we split the pair potential into repulsive and attractive parts. For the cut and shifted Lennard-Jones potential that we use in this work we have

$$\Phi(r) = \begin{cases}\Phi_{\rm LJ}(r) - \Phi_{\rm LJ}(r_c), & r<r_c\\ 0, & r>r_c\end{cases}, \tag{4}$$

$$\Phi_{\rm LJ} = 4\epsilon\left[\left(\frac{\sigma}{r}\right)^{12} - \left(\frac{\sigma}{r}\right)^{6}\right], \tag{5}$$

$$r_c = 2.5\sigma.$$

We follow Weeks *et al.*[29] and split the potential at the minimum, $r_{\rm min} = 2^{1/6}\sigma$. The repulsive potential is then linked to an equivalent hard sphere potential. The minimization of Eq. (1) with respect to $\rho(\mathbf{r})$ is carried out by substituting Eq. (3) into Eq. (1) and differentiating with respect to $\rho(\mathbf{r})$. The resulting Euler–Lagrange equation is solved numerically. Details of this procedure have been reported previously.[7] The LDA has been used extensively in the study of fluid–fluid interfaces (e.g., Ref. 30), wetting phenomena,[31] and capillary condensation.[1–10] It is expected to give good results when the variation in density is small over the range of the intermolecular interactions, as is the case for a fluid in a gravitational field for example. However, even for fluid–fluid interfaces where the density varies much more rapidly the results are generally good. It has been recognized, however, that LDA fails to predict the strong oscillations that are present in the density profile of a fluid in contact with a solid substrate. These oscillations are a reflection of short-ranged correlations in the fluid. The latter can be included in $\mathscr{F}_{\rm hs}[\rho(\mathbf{r})]$ and one way to do this is described below.

B. Smoothed density approximation (SDA)

To introduce the SDA we write,[24]

$$\mathscr{F}_{\rm hs}[\rho(\mathbf{r})] = \int d\mathbf{r}\, f_{\rm id}(\rho(\mathbf{r})) + \int d\mathbf{r}\,\rho(\mathbf{r})\Delta\psi_{\rm hs}(\tilde{\rho}(\mathbf{r})), \tag{6}$$

Where $f_{\rm id}(\rho(\mathbf{r}))$ is the ideal gas part of the free energy density and $\Delta\psi_{\rm hs}(\tilde{\rho}(\mathbf{r}))$ is the configurational (or excess) part of the free energy per particle, which we treat in terms of the smoothed density $\tilde{\rho}(\mathbf{r})$, i.e.,

$$\Delta\psi_{\rm hs}(\rho) = \frac{1}{\rho}[f_{\rm hs}(\rho) - f_{\rm id}(\rho)]. \tag{7}$$

We follow the description of Tarazona[24] and define a smoothed density

$$\tilde{\rho}(\mathbf{r}) = \int d\mathbf{r}'\,\rho(\mathbf{r}')w(|\mathbf{r}-\mathbf{r}'|;\tilde{\rho}(\mathbf{r})). \tag{8}$$

The weight function w is normalized,

$$\int d\mathbf{r}\, w(r) = 1 \tag{9}$$

and is assumed to have an expansion in powers of the smoothed density,

$$w(r;\tilde{\rho}(\mathbf{r})) = w_0(r) + w_1(r)\tilde{\rho}(\mathbf{r}) + w_2(r)\tilde{\rho}(\mathbf{r})^2 + \cdots. \tag{10}$$

The coefficients w_i can be estimated by comparing the density expansion of the direct correlation function $c_{\rm hs}(r;\rho)$, that results from the second functional derivative of the configurational free energy, with the Percus–Yevick result.[24] Including terms up to w_2 and substituting Eq. (10) into Eq. (8) gives a quadratic equation for $\tilde{\rho}(\mathbf{r})$ in terms of $\rho(\mathbf{r})$,

$$\tilde{\rho}(\mathbf{r}) = \tilde{\rho}(\mathbf{r}) + \tilde{\rho}_1(\mathbf{r})\,\tilde{\rho}(\mathbf{r}) + \tilde{\rho}_2(\mathbf{r})[\tilde{\rho}(\mathbf{r})]^2, \tag{11}$$

where

$$\tilde{\rho}_i(\mathbf{r}) \equiv \int d\mathbf{r}'\,\rho(\mathbf{r}')w_i(|\mathbf{r}-\mathbf{r}'|), \quad i=0,1,2. \tag{12}$$

The physical root of Eq. (11) is easily identified. The correct expressions for w_i, $i=0$, 1, 2 are given in Ref. 9. With the above prescription for $\tilde{\rho}(\mathbf{r})$ and inserting Eq. (6) into Eq. (1) we arrive at a similar minimization problem as in Sec. II A. The SDA has been tested with good results for a system of hard spheres against a hard wall for which computer simulation results are available.[24] It has been applied to study the solid–fluid transition and recently, Tarazona *et al.*[9] have reported results of the SDA in a variety of interfacial problems, notably wetting and capillary condensation of a Yukawa fluid in a slit geometry. In this paper we will apply both the SDA and the LDA to capillary condensation in a cylindrical pore and compare directly with extensive simulation results for the same model. In studying cylindrical pores it is natural to check how well the SDA can represent a fluid when the radius of the cylinder approaches zero. Tarazona *et al.*[9] have considered the equivalent limit in a slit geometry. Here we will adapt that approach to the one-dimensional fluid. Consider a three-dimensional density profile of the form

$$\rho(\mathbf{r}) = \rho^{\rm 1D}\delta(x)\delta(y). \tag{13}$$

Downloaded 09 Mar 2007 to 141.108.2.9. Redistribution subject to AIP license or copyright, see http://jcp.aip.org/jcp/copyright.jsp

This density produces a finite uniform one-dimensional density

$$\rho^{1D} = \frac{1}{L}\int d\mathbf{r}\,\rho(\mathbf{r}), \tag{14}$$

where $L = \int dz$ is the length in the z direction. For the nonideal part of the free energy functional (6) we then find

$$\Delta\mathscr{F}_{hs}[\rho(\mathbf{r})] = L\rho^{1D}\Delta\psi_{hs}(\tilde{\rho}(0)), \tag{15}$$

where $\tilde{\rho}(0) \equiv \tilde{\rho}(x=0, y=0)$ and $\Delta\psi_{hs}(\tilde{\rho}(0))$ represents the one-dimensional excess free energy per particle. One can calculate the smoothed density $\tilde{\rho}(0)$ from Eqs. (11) and (12) using $\rho(\mathbf{r})$ from Eq. (13). The approximation (15) to the one-dimensional free energy per particle is

$$\Delta\psi_{hs}(\tilde{\rho}(0)) = kT\,\tilde{\eta}(4-3\tilde{\eta})/(1-\tilde{\eta})^2, \tag{16}$$

where $\tilde{\eta} = (\pi/6)\tilde{\rho}(0)d^3$ and k denotes Boltzmann's constant and d the hard sphere diameter. This can be compared to the exact result for hard rods,

$$\Delta\mathscr{F}^{1D}_{HS}(\rho^{1D}) = -kT\ln(1-\rho^{1D}d). \tag{17}$$

For $\rho^{1D}d < 0.4$ Eq. (15) is within 10% of the exact result; above 0.4 the three-dimensional approximation overestimates the exact result. By differentiating Eq. (15) with respect to ρ^{1D} we can also compare the pressure with the exact result and we obtain the same level of agreement.

C. Comparing MFT and simulation

Comparison of mean field density functional theory (MFT) results with simulation is complicated by the underlying difference in bulk phase diagrams. The mean field equation of state

$$p = p_{hs} - \frac{\alpha}{2}\rho^2 \tag{18}$$

is the same for both LDA and SDA. Here $\alpha \equiv \int d\mathbf{r}\,\phi_a(r)$ is the integrated strength and p_{hs} is the hard sphere pressure. Different schemes have been employed for dividing the pair potential into repulsive and attractive parts. One scheme is to follow Barker and Henderson (BH) and split the Lennard-Jones potential at $r = \sigma$ and use the BH description for the equivalent hard sphere diameter. This approach is discussed by Fischer *et al.*[32] We have followed the WCA description[29] and split the potential at the minimum, and thus divide according to the forces rather than the potential. In our previous work[7,8,19] we have applied this with the Percus–Yevick hard sphere equation of state, for which a temperature-dependent hard sphere diameter was used[7,19,30]. In particular, we followed Lu *et al.*[30] and used a diameter that was fitted to give good agreement for coexisting densities between MFT and simulations. Note that this fit was aimed at low temperatures and in addition concentrated on the *full* LJ potential. In this paper we have again chosen the WCA prescription, but for convenience we kept the hard sphere diameter d equal to σ, thus ignoring the temperature dependence of d. The same choice was recently made by Bali and Evans.[33] For the hard sphere equation of state we employed the Carnahan–Starling expression. In Fig. 1 we compare the coexisting densities obtained by simulation with MFT. Results from both our previous prescription[7,8,19] and the current choice for the hard sphere diameter are shown. We have chosen to plot the densities as a function of T/T_c, where T_c is the appropriate critical temperature, since we will compare simulation and MFT for the pores according to this criterion. By doing so, we can make a better comparison for the capillary critical points that we find for the fluids in pores. The underestimation of the coexisting liquid densities is reflected in the slightly lower values for the liquid–vapor surface tensions, that we calculate using SDA and LDA. Whereas the bulk phase diagrams are the same, the surface tensions, γ_{LV}, will differ for these two approximations. The SDA results for the reduced surface tension $\beta_c\gamma_{LV}\sigma^2(\beta_c \equiv 1/kT_c)$ are slightly lower than those obtained for LDA. The calculated surface tension is compared in Table I with simulation data for the same model.[49,50] The difference in LDA and SDA is of importance when comparing the density functional results with the macroscopic Laplace or Kelvin equations. We note that LDA and SDA produce a similar difference for the Yukawa potential, and thus slightly larger than the result reported previously in Ref. 9.

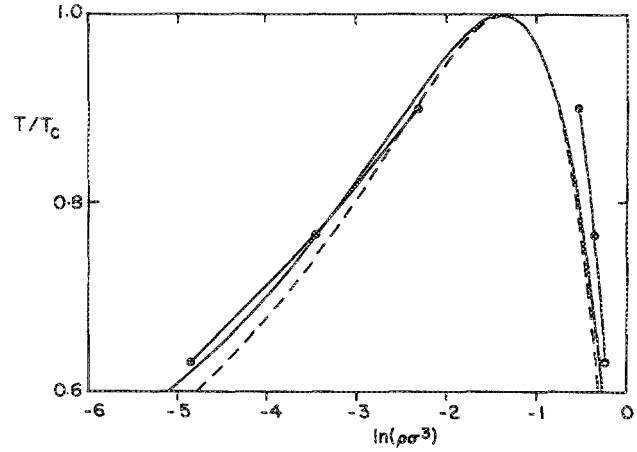

FIG. 1. Bulk coexistence diagram for a cut and shifted Lennard-Jones fluid, The full curve is the MFT result [Eq. (18)] for a temperature independent hard sphere diameter, $d = \sigma$. The dashed curve corresponds to MFT with a temperature dependent hard sphere diameter as used in Refs.7, 19, and 30. The open circles denote the simulation results.

D. The limit of small radius

When the pore radius becomes sufficiently small, we expect the fluid in the pore to show one-dimensional behavior. For small radii ($R^* \equiv R/\sigma \lesssim 2$) the external field that we use in this work[7] has a single minimum located at the pore axis, $r = 0$ (see Fig. 2). In this situation most particles will be located close to the pore axis. We can then define an effective one-dimensional density by

TABLE I. Liquid–vapor surface tensions.

	$\beta_c\gamma\sigma^2$		
T/T_c	Simulation	SDA	LDA
0.6306	0.53 (Ref. 49)	0.426	0.479
0.6757	0.43 (Ref. 49)	0.347	0.391
0.7207	0.38 (Ref. 49)	0.275	0.311
0.8108	0.20 (Ref. 50)	0.151	0.171

Downloaded 09 Mar 2007 to 141.108.2.9. Redistribution subject to AIP license or copyright, see http://jcp.aip.org/jcp/copyright.jsp

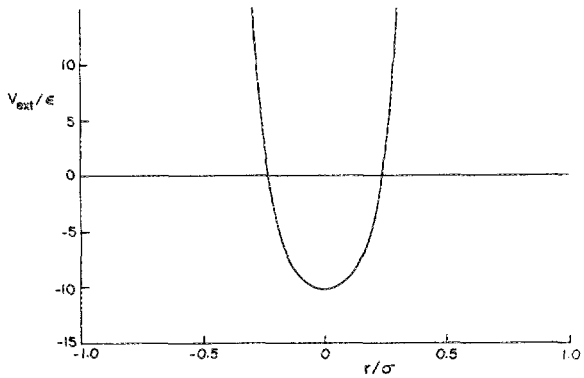

FIG. 2. The external potential for a cylindrical pore of radius $R^* = 1.0$, showing a single minimum. For clarity we have reflected the potential through the z axis. The distance from the pore axis is denoted by r. The potential diverges at $r^* = 1$.

$$\rho_{1D} \equiv \frac{N}{L} = \frac{1}{L}\int_{\text{pore}} d\mathbf{r}\, \rho(\mathbf{r}) = 2\pi \int_0^R dr\, r\rho(r), \qquad (19)$$

where L denotes the pore length and N the total number of particles in the pore. We will further assume that $\rho(r)$ is well represented by

$$\rho(r) = Ce^{-\beta V_{ext}(r)}. \qquad (20)$$

Here C is a normalization constant whose value follows from Eq. (19) as

$$C = \rho_{1D}/2\pi \int_0^R dr\, r \exp[-\beta V_{ext}(r)]. \qquad (21)$$

Thus we assume that the average radial distance of a particle's location from the pore axis is *independent* of the position of its neighbors and hence is identical to that of an ideal gas of N particles. This is a realistic approximation when the external field shows a single minimum and rises steeply away from the pore axis, i.e., whenever particles are unlikely to be able to slide past each other. In this limit we can easily obtain the adsorption isotherm from the potential distribution theorem[34,35]

$$\beta\mu = \ln \rho(r) + 3 \ln \Lambda + \beta V_{ext}(r) - \ln\langle e^{-\beta\phi(r)}\rangle, \qquad (22)$$

where Λ denotes the De Broglie wavelength. The last term of Eq. (22) indicates the fluid contributions felt by a test particle inserted at a distance r from the pore axis. This term can be identified as $-\beta\mu^{ex}_{1D}(\rho_{1D})$, the excess chemical potential of the one-dimensional fluid.

Substituting Eq. (20) into Eq. (22) we obtain [using Eq. (21)] for the configurational chemical potential

$$\begin{aligned}\beta\mu' \equiv \beta\mu - 3\ln\Lambda &= \ln\rho_{1D} - \ln I_1 + \beta\mu^{ex}_{1D}(\rho_{1D}) \\ &= \beta\mu_{1D}(\rho_{1D}) - \ln\Lambda - \ln I_1 \\ &\equiv \beta\mu'_{1D}(\rho_{1D}) - \ln I_1, \qquad (23)\end{aligned}$$

where I_1 denotes the denominator of Eq. (21). $\ln I_1$ represents the constant by which the chemical potential of the 1D fluid in the pore is shifted. To calculate the right-hand side of Eq. (23) we might use WCA perturbation theory[29] for a one-dimensional fluid, which is slightly simpler[36] to apply than its 3D counterpart since $g(r)$ is known exactly for the reference system of hard rods,[36,37] as is the equation of state.[38,39] We have followed Bishop[36] in our calculation of the Helmholtz free energy, but obtain the pressure, and hence $\mu'_{1D}(\rho_{1D})$, by differentiating the free energy with respect to volume rather than using the pressure equation.[36] This leads to much better agreement with simulation results for the same system.[40] Of course, for the exact $g(r)$ the two routes are equivalent, but in the perturbation theory approximation this thermodynamic consistency is lost. One obvious defect of perturbation theory, in common with mean field theory, is that it produces a critical point, while it is well known that a one-dimensional system with finite ranged interactions does not show a phase transition at any nonzero temperature (e.g., Ref. 41). We shall compare the perturbation theory results with a direct simulation for a radius $R^* = 1$.

For a pore consisting of two parallel plates, the small separation limit, $H \to 0$, produces a two-dimensional system. This limit was discussed by Tarazona *et al.*[9] Defining a 2D effective density $\rho_{2D} = \int_0^H dz\, \rho(z)$ we obtain the following result, similar to the 1D limit [cf. Eq. (23)]:

$$\beta\mu' = \beta\mu'_{2D}(\rho_{2D}) - \ln I_2, \qquad (24)$$

where $I_2 \equiv \int_0^H dz \exp[-\beta V_{ext}(z)]$ and $\beta\mu'_{2D}(\rho_{2D}) \equiv \beta\mu_{2D}(\rho_{2D}) - 2\ln\Lambda$. Again, we could use perturbation theory or simply mean field theory to calculate the properties of a 2D fluid, i.e., to obtain the right-hand side of Eq. (24). The same treatment can be applied to a fluid adsorbed onto a single wall. This was considered by Knight and Monson.[51] For temperatures below the two-dimensional critical temperature, T_c^{2D}, the fluid will show 2D liquid–vapor coexistence[9] in the limit $H \to 0$. Using a mean field approximation we can easily calculate the coexisting properties of the 2D fluid for $T < T_c^{2D}$. From Eq. (24) we obtain the corresponding 3D bulk phase properties, and hence locate the capillary condensation point. Thus, capillary condensation in a slit geometry, in contrast to a cylindrical pore, will occur even in the limit $H \to 0$ when $T < T_c^{2D}$.[9]

III. SIMULATION METHODS

Molecular dynamics and grand canonical Monte Carlo simulations have several differences though both are useful in the study of adsorption phenomena. An MD program simulates a system in the microcanonical (NVE) ensemble, and with temperature scaling, the canonical (NVT) ensemble. If the number of particles and volume are chosen for the pore such that the overall density falls in the two-phase region, a gas/liquid interface will form. GCMC, on the other hand, is designed to simulate a system in the grand ensemble (μVT). Any gas/liquid interface found in the GCMC simulations would not correspond to an absolute minimum in Ω even if the chemical potential is fixed exactly at the coexistence value. As a result, the configuration of the system will be either that of a gas or a liquid, but not both. Both methods can be used to find coexistence between competing phases in a confined system. In this section we briefly describe the two methods while referring the interested reader to previous publications[18,19] for full details.

All the simulations were performed for a fluid interacting via the cut and shifted LJ potential, Eqs. (4) and (5). A one-body external field represents the interactions between

Downloaded 09 Mar 2007 to 141.108.2.9. Redistribution subject to AIP license or copyright, see http://jcp.aip.org/jcp/copyright.jsp

the solid and fluid molecules. The interactions are averaged over a solid of uniform density ρ_s,

$$V_{\text{ext}}(\mathbf{r}) = \rho_s \int_{\text{solid}} d\mathbf{r}'\, \Phi_w(|\mathbf{r}-\mathbf{r}'|, \epsilon_w, \sigma_w), \tag{25}$$

where ϕ_w is the full LJ potential characterized by σ_w and ϵ_w. The parameters were taken as $\epsilon_w/\epsilon = 1.277$, $\sigma_w/\sigma = 1.094$ and $\rho_s\sigma_w^3 = 0.988$, which approximate fluid argon interacting with a carbon dioxide wall.[18,19] The integral in Eq. (25) can be partially performed to yield an external field that varies only with the radial distance r from the pore axis.

The MD method employs Verlet's Leap Frog algorithm[42] to solve the equations of motion and the algorithm of Brown and Clarke[43] to keep the temperature constant. Each state point was equilibrated for a length of time sufficient to remove effects of the starting configuration and then averages were accumulated. The number of particles used varied from 356 for $R^* = 2.5$, 1560 for $R^* = 5$, to 3891 for $R^* = 7.5$. Averages were taken over at least 50 000 time steps of $0.005\,(m\sigma^2/\epsilon)^{1/2}$ for $R^* = 2.5$ and 25 000 timesteps for $R^* = 7.5$. Often much longer runs were performed. By dividing the pore into bins, both radial and axial, and averaging the number of particles in each bin, the complete density distribution was obtained.[18] Bin sizes ranged from 0.05σ (radial) to 0.2σ (axial). Similarly, by inserting particles randomly and uniformly in these same bins, one can obtain the chemical potential profile using the potential distribution theorem.[34,35] For an inhomogeneous fluid we have

$$\beta\mu = \ln\rho(\mathbf{r}) + 3\ln\Lambda - \ln(\langle\exp\{-\beta\,[U(\mathbf{r}) + V_{\text{ext}}(\mathbf{r})]\}\rangle), \tag{26}$$

where $U(\mathbf{r})$ is the potential energy felt by an additional test particle inserted at $\mathbf{r}$, due to all the fluid particles. The angular bracket denotes a time average. We accumulated a profile of the right-hand side of Eq. (26) as a function of r and z in the same sized bins as we used for the density profile. The constancy of the right-hand side throughout the pore is a requirement for equilibrium. Heinbuch and Fisher[11,13] have recently suggested an integrated form of Eq. (26) that can be used for inhomogeneous fluids, but which relies on the uniformity of the chemical potential.

The chemical potential for a fully equilibrated pore with coexisting gas and liquid gives the location of the true transition between those phases, while the complete density profile allows one to examine the meniscus formed at the gas/liquid interface.

The Monte Carlo method[19] was based on that of Adams.[44] Each new configuration was generated by first attempting the movement of a particle and then attempting either the insertion or deletion of a particle. The number of particles and the configurational energy were averaged over several million configurations following at least one million initial configurations which were discarded. Generally the pore length used was 10σ. The radial density profile was obtained as in the MD simulations. For given μ, V, and T two states could sometimes be found (gas-like and liquid-like) for two different initial conditions. The grand potential can be found from the simulations via thermodynamic integration.[19] Along an adsorption isotherm we use the Gibbs adsorption equation at fixed volume V and area A,

$$\left(\frac{\partial\Omega}{\partial\mu}\right)_{T,V,A} = -\int d\mathbf{r}\,\rho(\mathbf{r}) = -N. \tag{27}$$

Along the gas branch Eq. (27) can be integrated from a low density reference point where we can assume ideal gas behavior and thus calculate Ω. To locate the phase transition one needs Ω along the liquid branch. For this we have to construct a reversible path that connects the liquid branch with the reference point. We use[19]

$$\left(\frac{\partial(\Omega/T)}{\partial(1/T)}\right)_{\mu,V,A} = E - N\mu \tag{28}$$

along a path of constant chemical potential to calculate Ω for a point located on an isotherm which is supercritical with respect to the capillary critical temperature. In Eq. (28) E denotes the total internal energy. Along the supercritical adsorption isotherm, we integrate Eq. (27) up to a chemical potential that is sufficiently large so that Eq. (28) can be integrated once more to produce Ω on the liquid branch of the isotherm of interest. The chemical potential of the phase transition then follows from equating the grand potential along the gas and liquid branch. This route for finding the transition is complementary to the direct method (NVT) and this provides a powerful check on the consistency of both methods. The simulation data are summarized in the Appendix.

IV. RESULTS AND DISCUSSION

A. Structure

One of the chief aims of any theory for confined fluids is to predict the structure of the fluid. In this section we present a discussion of the structure obtained by two types of simulation, MD and GCMC, and that produced by the LDA and SDA. Recent simulation studies have determined the structure of both the gas and liquid regions of a fluid confined to a small pore.[18,19,22] Peterson and Gubbins[19] compared the fluid structure predicted by the LDA to that predicted by GCMC and Heffelfinger *et al.*[18] investigated the liquid/vapor interface. Ball and Evans[33] have recently compared density profiles from the SDA with computer simulation results.[22] We note that the SDA calculations by Ball and Evans[33] were performed for a cutoff that was smaller than that used in the simulation.

In Fig. 3 we show a series of radial density profiles from GCMC for a pore of radius $R^* = 2.5$. This series gives the structure in the pore along the $T/T_c = 0.631$ adsorption isotherm. Here and below we have reduced the simulation results by the bulk critical temperature, $T_c^* \simeq 1.11$. Similarly we reduce the mean field results by the corresponding critical temperature which is $T_c^*(\text{MF}) = 1.23$ for the approximation that we use in this work. The first plots [Figs. 3(a) and 3(b)] are radial density profiles for gas-like states while the latter plots [Figs. 3(c) and 3(d)] are those of high density, liquid states. The gas profiles shown in Figs. 3(a) and 3(b) are quite flat near $r = 0$, indicating that for this density, the fluid at the center of the pore behaves as in the bulk. The position and height of the peak near the wall is determined by the location and depth of the attractive well of the fluid–

Downloaded 09 Mar 2007 to 141.108.2.9. Redistribution subject to AIP license or copyright, see http://jcp.aip.org/jcp/copyright.jsp

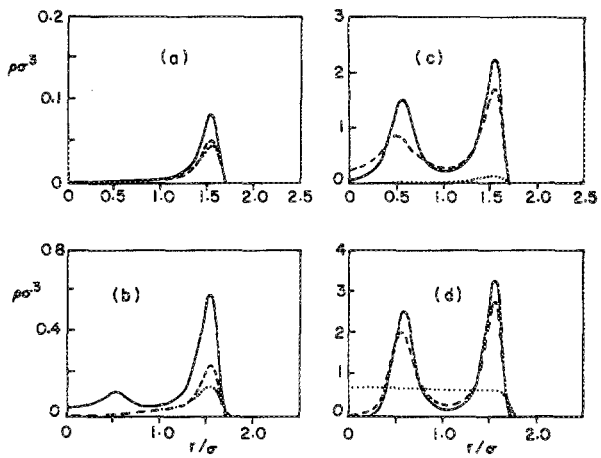

FIG. 3. Radial density profiles for $R^* = 2.5$ and $T/T_c = 0.631$. The solid lines are from GCMC, the dashed lines are from the SDA, and the dotted lines are from the LDA. (a) $P/P_{sat} = 0.029\,39$. (b) $P/P_{sat} = 0.1033$ (gas). (c) $P/P_{sat} = 0.1033$ (liquid). (d) $P/P_{sat} = 0.5212$.

wall potential. The shape of these low density profiles resembles that of an ideal gas in the external field. The radial density profile for a gas near the transition, Fig. 3(b), exhibits a small second peak. This peak is due to the increasing effect of interparticle interactions and usually indicates proximity to the transition. In Figs. 3(c) and 3(d), the structure of the liquid is shown. These can be understood as one large peak adsorbed on the wall, with the particles of the second smaller peak adsorbed on the particles composing the first peak. Also shown in Fig. 3 are the results for the LDA and SDA. It is seen that as the density in the pore increases the LDA fails to describe the structure even qualitatively. The SDA, on the other hand, gives a good representation of the liquid structure. Just below the transition [Fig. 3(b)] the agreement is less good. This is a consequence of the fact that we compare simulation and theory at the same value of P/P_{sat}. The differences in the bulk phase diagrams (see Sec. II C) will lead to differences in the relative pressure at which capillary condensation occurs. The stronger variation of the adsorption (see also Fig. 7 below) close to the transition is thus amplified in the gas density profiles. The adsorption isotherms are discussed in detail in the next section. Other methods of comparison are also possible. For instance Ball and Evans[33] compare simulation and theory profiles at one pressure, namely the capillary condensation pressure. In principle one could use this pressure, rather than the bulk pressure, to reduce the data along the isotherm.

The GCMC radial density profiles in Fig. 3 demonstrate the structure of the liquid and gas regions of the fluid confined to the pore. A liquid/vapor interface will not appear in the GCMC simulations since a system with an interface would not correspond to a minimum in the grand potential. Due to this constraint, the nature of the interface must be investigated using simulations employing a constant number of particles, as in MD. In Fig. 4(a) is shown the full density profile for the coexisting phases in the pore at a series of temperatures for $R^* = 2.5$. The liquid structure is seen as bands of high density fluid. These bands correspond to the

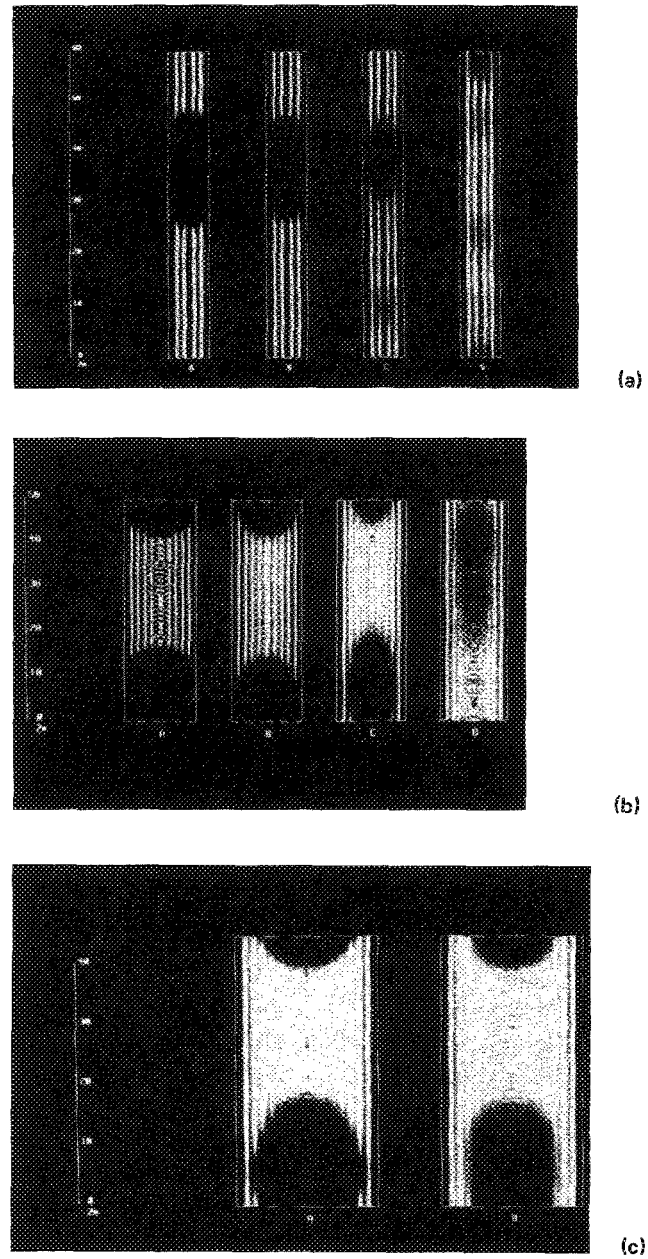

FIG. 4. Density profiles for a Lennard-Jones fluid in a cylindrical pore. The profile was plotted by assigning an intensity proportional to the density at (r, z) and shading. (a) $R^* = 2.5$, from left to right the temperature increases from $T/T_c = 0.541, 0.586, 0.631$, to 0.649. (b) $R^* = 5.0$, from left to right the temperature increases from $T/T_c = 0.450$, 0.631, 0.766, to 0.901. (c) $R^* = 7.5$, $T/T_c = 0.631$ (left) and $T/T_c = 0.766$ (right).

peaks in the radial density profile produced by GCMC. The gas comprises the dark region in this figure. Note that for clarity we have reflected the profile through the z axis. MD radial density profiles for the gas and liquid portions of the full density profile match those of GCMC. At the highest temperature, $T/T_c = 0.649$, the system is very close to and probably just below the capillary critical point. Just above the capillary critical point we typically observe large fluctuations and no stable interface.[18] Figure 4(b) shows the full profile for a radius of $R^* = 5$ and four different temperatures, of which the last one is above the capillary critical

Downloaded 09 Mar 2007 to 141.108.2.9. Redistribution subject to AIP license or copyright, see http://jcp.aip.org/jcp/copyright.jsp

point. With increasing temperature the gas layer near the wall grows and the menisci clearly broaden. Similar results are shown for a radius of $R^* = 7.5$ in Fig. 4(c). By now the radius is sufficiently large so that the strong structural bands seen in Figs. 4(a) and 4(b) have died away. For the highest temperature one can clearly see a second peak in the gas region. This leads to an increased adsorption, an effect which is discussed in more detail in Sec. IV C.

The full density profile may also be used to calculate the radius of curvature of the meniscus, facilitating comparison of the simulation results with the predictions of the Kelvin equation. This has been done previously for a radius of $R^* = 5.0$.[18,19]

In Fig. 5 are shown density profiles from simulation for several pore radii; all are at $T/T_c = 0.631$ and at $P = P_{sat}$, the *bulk* saturation pressure, where the liquid is the stable phase in the pore. For $R^* = 1.0$ the structure consists simply of a highly localized row of fluid atoms at the center of the pore. $R^* = 2.5$ allows 2 annuli of particles to form, while $R^* = 5.0$ allows 4 annuli with a center row similar to the $R^* = 1.0$ profile. The relatively high peak corresponding to this row of molecules is peculiar to cylinders and has been discussed in previous work.[4,9,18,19,22] For $R^* = 7.5$ one can see the usual liquid structure near the wall, but in the center of the pore, the fluid has a nearly constant density which is slightly above that of the bulk liquid.

In Fig. 5 is also shown the comparison between LDA, SDA, and GCMC for the four different radii. Again, the LDA radial density profile misses the structure details and appears to reflect the "average" behavior of the fluid in the pore. The radial density profiles predicted by SDA, on the other hand, follow the simulation results quite closely for the three larger pores, but fail to predict even the qualitative behavior for $R^* = 1.0$. A pore this small is a very stringent test for the SDA. In addition, the bulk condition $P = P_{sat}$ corresponds to an extremely high one-dimensional density, N/L. At these high densities the SDA overestimates the free energy of the reference fluid by a very large amount (see Sec. II B). It is also worthy of note that for the larger pores, the peaks from SDA, other than the one at the wall, are slightly shifted away from the peaks from simulation. This is due to our choice of a hard sphere diameter for the reference fluid, $d = \sigma$ at all temperatures. The value of d in WCA perturbation theory is very close to σ for the liquid densities along the bulk coexistence curve. Ball and Evans[33] have also used the same prescription for d. The influence of temperature is rather small and can be assessed from Fig. 6 where we show the comparison of simulation and mean field theory at two temperatures, $T/T_c = 0.541$ and $T/T_c = 0.631$.

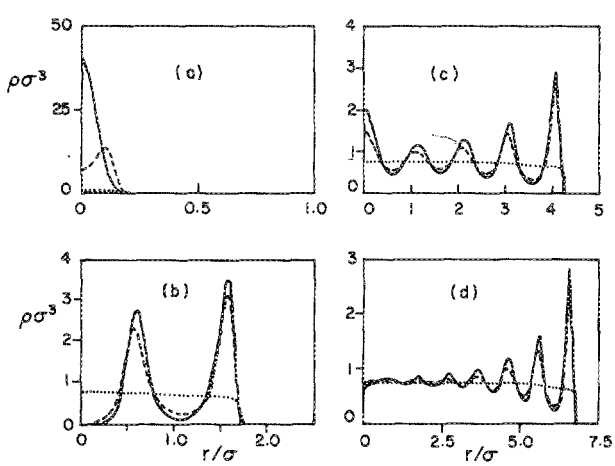

FIG. 5. Radial density profiles for $T/T_c = 0.631$ and $P/P_{sat} = 1.0$. Key as in Fig. 3. (a) $R^* = 1.0$. (b) $R^* = 2.5$. (c) $R^* = 5.0$. (d) $R^* = 7.5$.

B. Adsorption

Experimental studies of adsorption phenomena commonly focus on adsorption isotherms; plots of the amount of fluid adsorbed in a porous solid vs the pressure of the coexisting bulk gas. This information is also obtainable from the simulations and the density functional theories and in this section we compare the results from these methods. The simulations give directly the number of particles in the pore, and we have chosen to plot the average density $\bar{\rho} \equiv N/V$ vs the relative pressure p/p_{sat}. The volume V constitutes here that part of space where the external field is finite. The continuum density functional theories produce the radial density profile which we integrate to find the average density

$$\bar{\rho} = \frac{2}{R^2} \int_0^R \rho(r) r \, dr. \tag{29}$$

In Figs. 7 through 9 we give adsorption isotherms for three radii and various temperatures. Each of the plots contain the

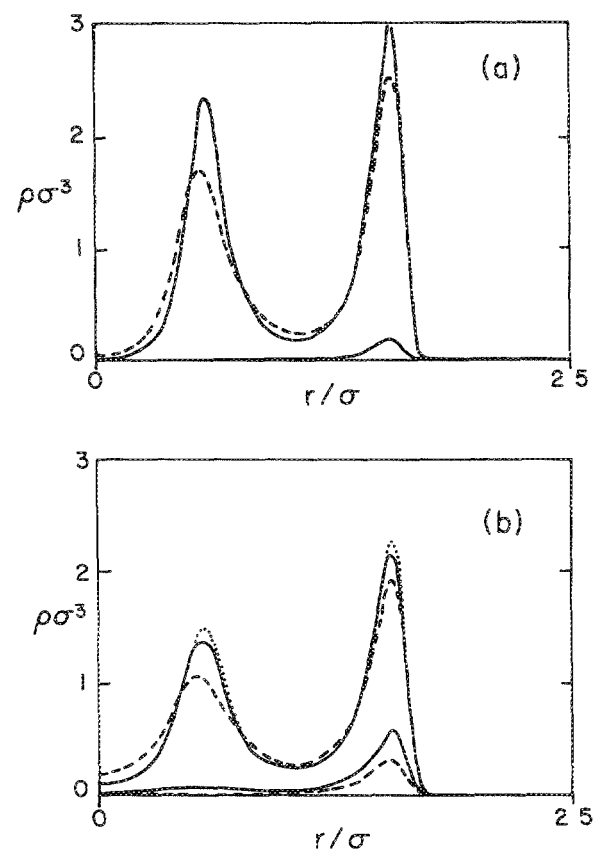

FIG. 6. Gas and liquid radial density profiles at the transitions for $R^* = 2.5$. (a) $T/T_c = 0.541$. The solid line denotes simulation (MD) and the dashed line is the SDA result. (b) $T/T_c = 0.631$. Key as in (a) and the dotted line denotes GCMC results.

Downloaded 09 Mar 2007 to 141.108.2.9. Redistribution subject to AIP license or copyright, see http://jcp.aip.org/jcp/copyright.jsp

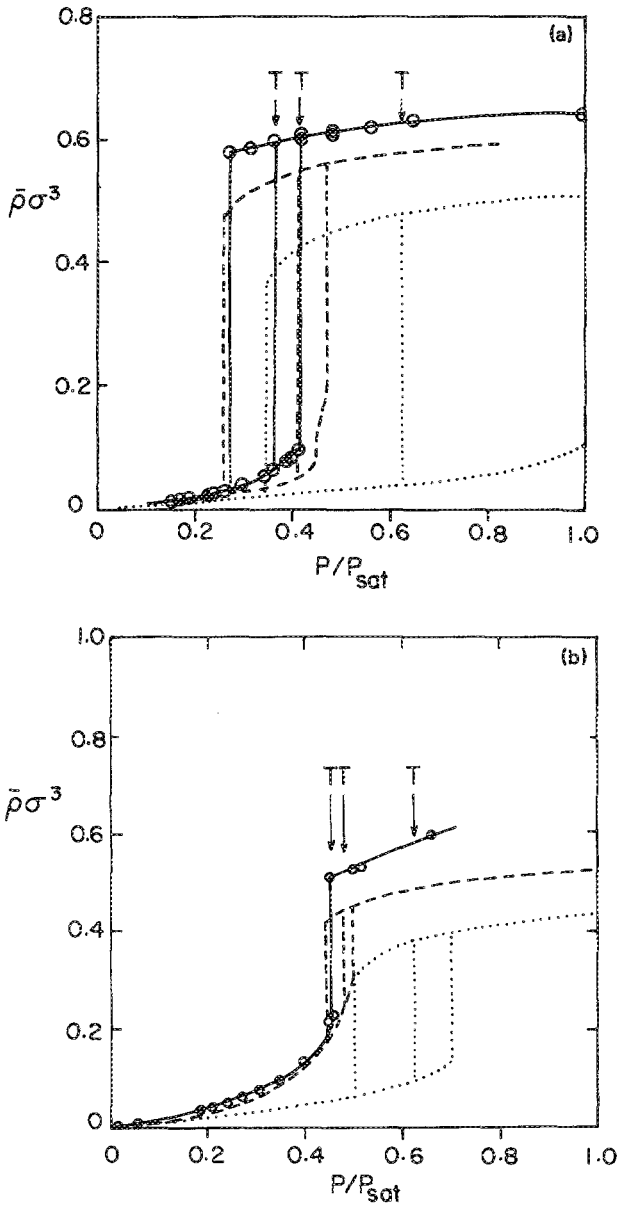

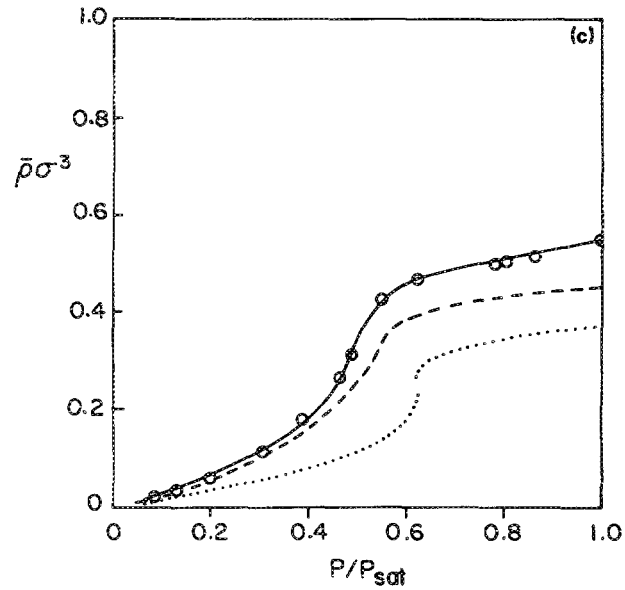

FIG. 7. Adsorption isotherms for $R^* = 5.0$; average density [see Eq. (29)] vs relative pressure, from GCMC (— and O), SDA (---), and LDA (···). For each of the three sets of results there are three vertical lines near the phase transition (a) and (b). The line in the center shows the true thermodynamic phase transition (marked T), and the lines to the right and left show the apparent transitions (hysteresis effect) on adsorption and desorption, respectively. (a) $T/T_c = 0.631$. (b) $T/T_c = 0.766$. (c) $T/T_c = 0.901$. The isotherm in (c) is just below the capillary critical point.

GCMC, LDA, and SDA results. Also shown are the MD results for the transition in Figs. 7(a), 7(b), and 8. Consider the simulation results shown in Fig. 7 for three temperatures (all below the bulk critical temperature) in a pore of radius 5.0σ. The lowest temperature result shows two distinct branches corresponding to gas- and liquid-like states in the pore. Each branch has stable and metastable portions separated by a transition between the two branches. The position of this capillary condensation transition was found through calculations of the grand potential[19] (GCMC) or the chemical potential[18] (MD). The results at $T/T_c = 0.766$ ($T^* = 0.85$) are similar, but the metastable portions of the isotherm are very small. This shows that this temperature is just under the capillary critical point for the transition. $T/T_c = 0.901$ ($T^* = 1.0$) is clearly above this critical point (but still below the bulk critical point) as the isotherm is single valued over its entire range. No phase separation was found in the MD simulations[18] at this temperature.

The density functional results are also shown in Fig. 7. The SDA gives lower densities than the simulations at the

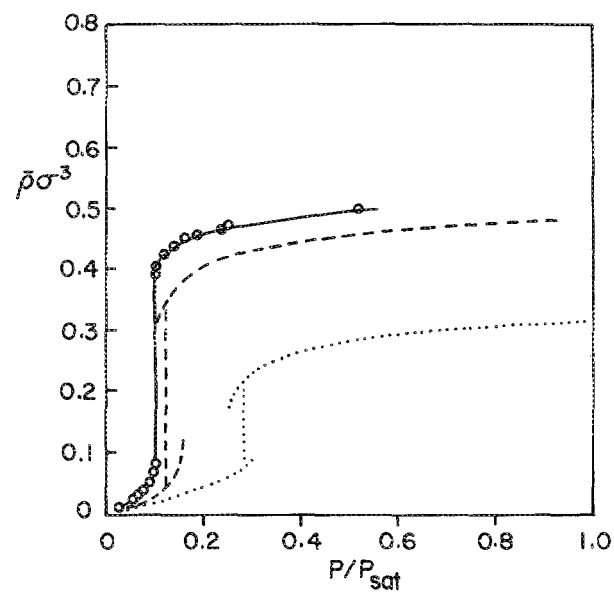

FIG. 8. Adsorption isotherm for $R^* = 2.5$ and $T/T_c = 0.631$. Key as in Fig. 7.

Downloaded 09 Mar 2007 to 141.108.2.9. Redistribution subject to AIP license or copyright, see http://jcp.aip.org/jcp/copyright.jsp

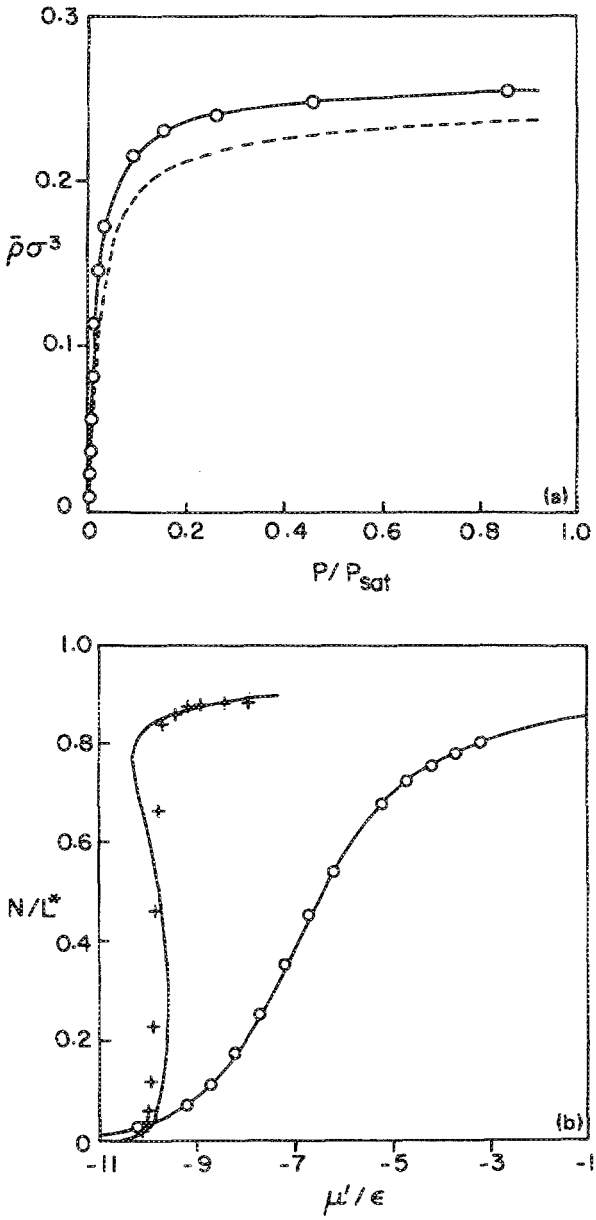

FIG. 9. Adsorption isotherms for $R^* = 1.0$. The quasi-one-dimensional case. (a) Average density [see Eq. (29)] vs relative pressure. GCMC (open circles); one-dimensional perturbation theory (solid line); SDA (dashed line). (b) Number of particles per unit (reduced) length vs configurational chemical potential. GCMC at $T^* = 0.2$ (pluses); GCMC at $T^* = 1.0$ (open circles); one dimensional perturbation theory (solid lines).

same relative temperature, T/T_c. The position of the first order transition or the steep portion of the supercritical isotherms are at slightly higher P/P_{sat} than in the simulations, but are represented much better than in the less accurate LDA. The lower adsorptions for liquids predicted by SDA are manifestations of the lower local densities shown in Figs. 3 and 5, and are a result of the mean field approximation. In Fig. 7(c), at $T/T_c = 0.901$, it can be seen that the LDA is slightly below the critical point for the pore transition while the SDA and simulation are above it. The lengths and positions of the metastable parts of isotherms are also very well represented by the SDA. In Fig. 7(a), however, the SDA result exhibits complicated behavior along the metastable portion of the gas branch. There are two very steep portions which appear to be regions where the first and second peaks in the density profiles are growing rapidly. These appear to be similar in nature to the layering transitions found in the density functional calculations of a confined lattice gas,[45] but in this case they are not first order transitions. They are apparently above the critical point (for the lattice gas Bruno *et al.*[45] find $T_c^{1t} \simeq T_c^{2D} \simeq 0.5T_c$) for such transitions.

As was shown previously[19] the LDA overestimates the condensation pressure compared to the simulations. The much lower liquid densities result from the failure of the LDA to exhibit any of the structure that results from the repulsive cores of the molecules. This affects not only the adsorption of the system but the energy and the free energy as well. The simulations show a higher density near the wall which leads to a larger (more negative) energy and thus a more stable liquid for a given pressure. Thus the high peaks at the wall stabilize the liquid to greater undersaturations compared to the LDA, for which the peaks are small. Hence, the transition between liquid and gas is at a lower pressure for the simulations, and also for the SDA, which predicts this aspect of the structure correctly.

In Fig. 8 we show an isotherm for $T/T_c = 0.631$ and $R^* = 2.5$. The density profiles in Fig. 3 correspond to points on this plot. The isotherm is qualitatively similar to the $T/T_c = 0.766$ isotherm for the $R^* = 5.0$ pore in that the metastable portions are very short and only one point was found in the simulations where both gas and liquid states persisted as metastable states. Comparing Fig. 8 to Fig. 7(a), which is at the same temperature, we can see that the critical point will be lower for the smaller pore. The relationship of the LDA and SDA results to those of the GCMC is similar to the $R^* = 5.0$ case.

Figure 9 contains isotherms for a pore with $R^* = 1.0$. Because only one particle can realistically fit in the cross section of such a pore, it is a quasi-one-dimensional system and therefore a limiting case worthy of investigation. The $T^* = 1.0$ isotherm in Fig. 9(a) is plotted vs the relative pressure as in Figs. 7 and 8. Its shape is like that of many experimental adsorption isotherms for fluids in solids with small pores. In Fig. 9(b) the number of molecules per unit length is plotted vs the chemical potential. The $T^* = 1.0$ isotherm gradually increases on this plot. The $T^* = 0.2$ isotherm exhibits a very steeply rising portion connecting low and high density states, but is still continuous. This lack of a first order transition at even extremely low temperatures is characteristic of a one-dimensional system. The results of the one-dimensional perturbation theory (see Sec. II D) are also shown on this plot. The perturbation theory predicts the higher temperature isotherm very accurately. However, being essentially similar to a mean-field theory, it predicts a loop at lower temperatures. The position of the steep portion in the simulation results falls within this loop.

C. Phase diagrams

In this section we present phase diagrams for the fluid–pore system as well as for the bulk fluids. As in the previous sections, the LDA and SDA theories are compared to the GCMC and MD simulation results. The fluid–pore system is similar to the bulk fluid, but with one more relevant variable;

Downloaded 09 Mar 2007 to 141.108.2.9. Redistribution subject to AIP license or copyright, see http://jcp.aip.org/jcp/copyright.jsp

the radius. This variable ranges from the one-dimensional case of $R^* \simeq 1.0$ to the bulk case of $R^* = \infty$. Evans *et al.*[5] have previously given results for phase diagrams in the variables 1/width, T/T_c, and P/P_{sat} for fluids contained in slits.

One way of portraying the gas–liquid coexistence region for a bulk fluid is with a temperature vs density plot. However, due to the nature of the external field in the pore, one finds difficulty in defining the volume and hence "the density" for a confined fluid. This is because the fluid is localized by the repulsive part of the external potential, and the extent of this localization depends on the temperature and other variables of the system.[46] We have chosen to define the volume by choosing the radius as the point where the external field diverges to infinity. The density is then defined as in Eq. (29).

In Fig. 10(a) we give the LDA results for the temperature vs the densities of the coexisting phases. Since some of the volume of the pore is essentially inaccessible to the fluid, the densities for the confined liquids are lower than for the bulk liquid at the same temperature. The densities of the gases are larger than their bulk counterparts because of the attractive nature of the potential. The excluded volume is a relatively larger proportion of the total for smaller pores and this causes the coexistence curves for smaller radii to lie within those for larger radii, at least for low temperatures. For higher temperatures and larger pores, the gas develops high density regions near the wall and this increases the average density in the pore. This moves the gas side of the coexistence curve to the right as is exhibited most clearly by the $R^* = 7.5$ curve. This phenomenon will be discussed further for the SDA and simulation results below.

The critical temperatures for the confined fluids are easily seen in Fig. 10 as the temperatures where the densities of the gas and liquid states become identical. The critical temperature is seen to decrease with pore radius.

The coexistence curves from the SDA [Fig. 10(b)] exhibit the same characteristics as those from the LDA, but the effect of the high density gases is more dramatic. The SDA allows higher peaks in the density profile than for the LDA (see Fig. 5) as discussed in Sec. IV B and these lead to higher average densities for the gas. This effect is enhanced by the cylindrical geometry; the factor of r in Eq. (29) emphasizes the contribution near the wall where the density is greatest. The strong increase of the coexisting gas density with temperature is a consequence of the rapidly increasing portion of the adsorption isotherm moving toward the condensation pressure as the temperature rises. This is shown in Figs. 11(a) and 11(b) for a pore of radius 5σ. An adsorption isotherm from simulation, for $R^* = 7.5$, showing the transition from a gas with multiple layers adsorbed on the wall to the liquid is also shown in Fig. 11(c). The sharp increases are clearly reflected in the density profile. In Fig. 12 we plot a series of density profiles in the neighborhood of the transition. Each profile is separated by equal steps in pressure and they correspond to the adsorption isotherm shown in Fig. 11(a). (It is tempting to argue that for large radii the flat part of the $T, \bar{\rho}$ curve would develop into a separate coexistence curve. In fact, the flattening that we observe occurs at $T/T_c \simeq 0.6$, which is close to the ratio of the two-dimension-

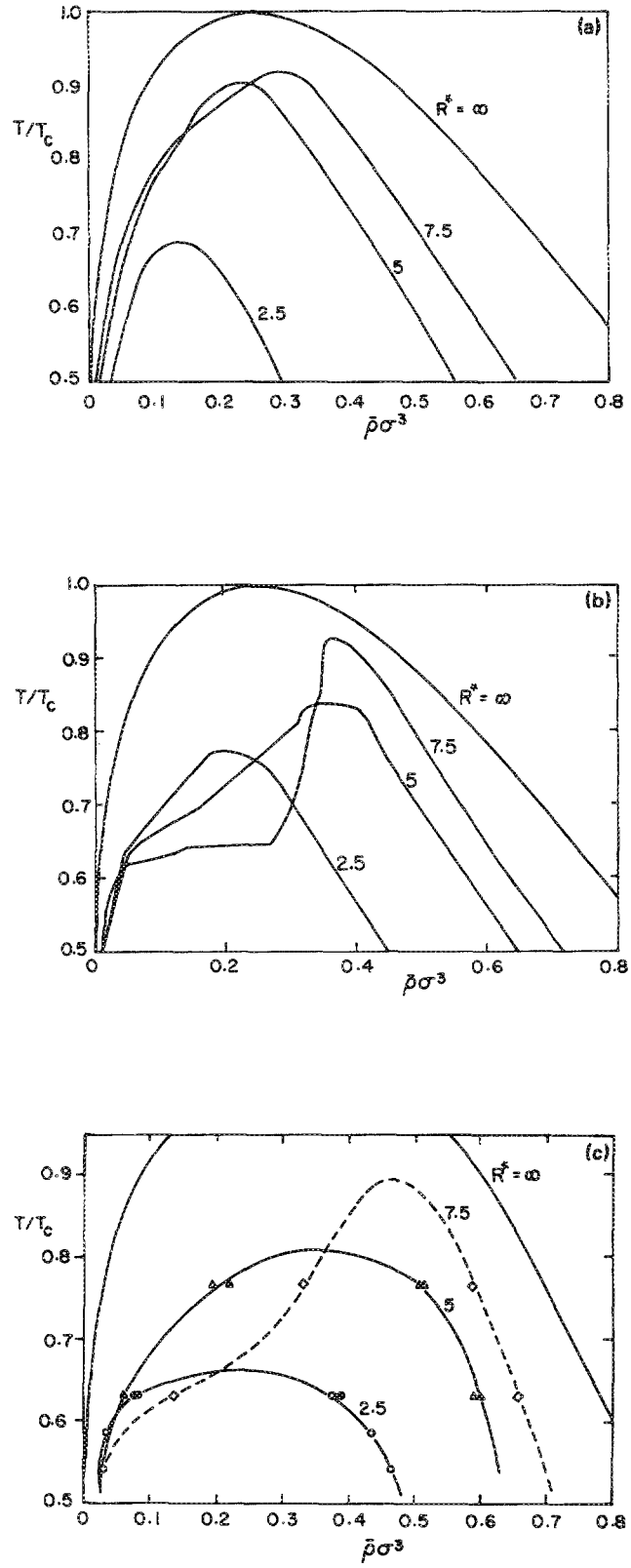

FIG. 10. Coexistence diagrams for the confined fluid. Relative temperature versus the average density [Eq. (29)]. (a) LDA. (b) SDA. (c) Simulation. Open symbols correspond to MD and closed symbols refer to GCMC results: $R^* = 2.5$ (circles), $R^* = 5.0$ (triangles), $R^* = 7.5$ (diamonds). The curve labeled $R^* = \infty$ corresponds to the bulk fluid. The dashed curve connecting the simulation results for $R^* = 7.5$ (c) is drawn with the SDA result of (b) as a guide.

Downloaded 09 Mar 2007 to 141.108.2.9. Redistribution subject to AIP license or copyright, see http://jcp.aip.org/jcp/copyright.jsp

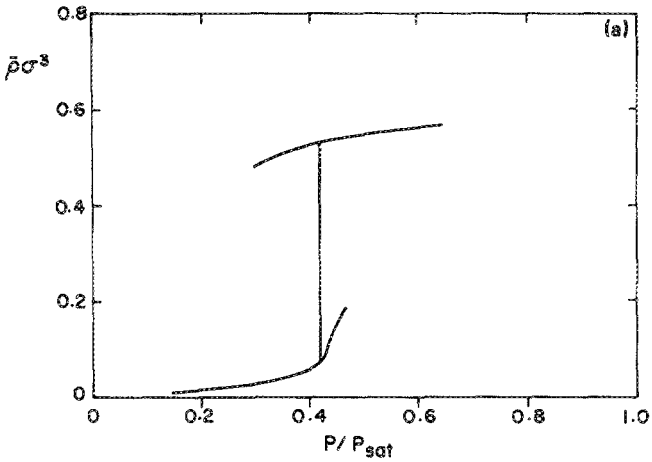

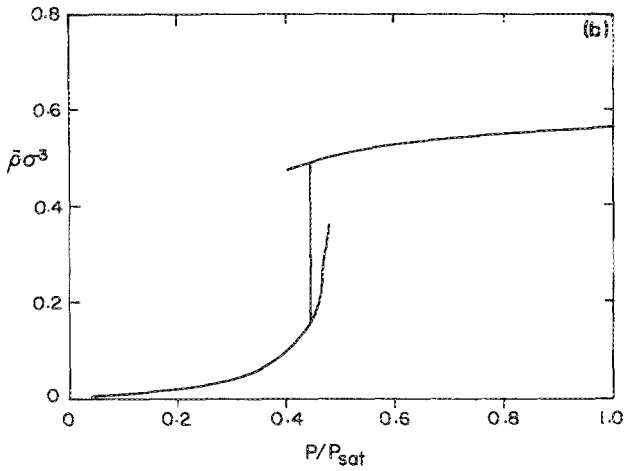

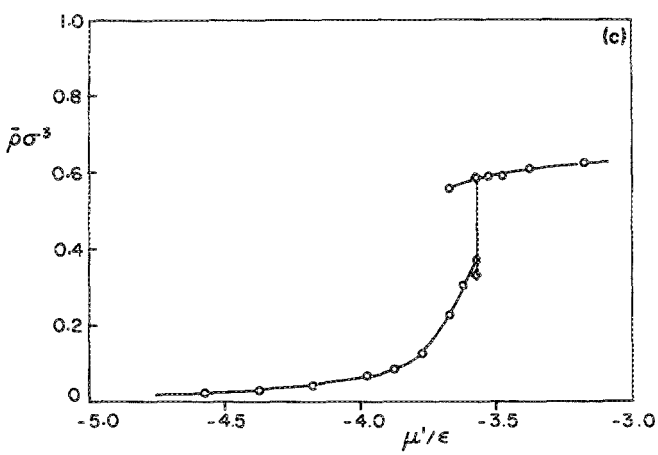

FIG. 11. Adsorption isotherms showing influence of high density gas states. (a) SDA at $R^* = 5.0, T/T_c = 0.650$. (b) SDA at $R^* = 5.0, T/T_c = 0.699$. (c) GCMC at $R^* = 7.5, T/T_c = 0.766$. Here the diamonds show the transition as determined by MD.

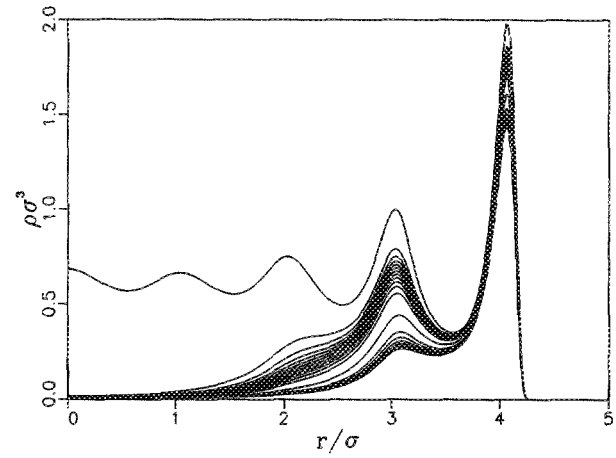

FIG. 12. Radial density profiles from the SDA for $R^* = 5.0$ and $T/T_c = 0.699$. The profiles correspond to the stable and metastable parts of the gas branch shown in Fig. 11(b). There are twenty curves for pressures from $P/P_{sat} = 0.4$ to $P/P_{sat} = 0.495$ in increments of 0.005.

al and three-dimensional critical temperatures: $T_c^{2D}/T_c^{3D} = 0.5618$. Such an extra lobe to the coexistence area would also occur when there is a competition between layering transitions[45] or prewetting[3] and capillary condensation. A similar suggestion was made by Chalupa and Huberman[47] although these authors did not find a proper capillary critical point.)

Simulation results from GCMC and MD are shown in Fig. 10(c). However, the capillary critical points for the simulations seem to be below those of the SDA.

Another method of presenting the phase equilibrium results is to plot the temperature against the density of the bulk fluid in equilibrium with the fluid–pore system. This bulk density is always that of a gas here, as our potentials induce the liquid/vapor transition at pressures below saturation for all temperatures studied. The corresponding bulk density is calculated by determining the chemical potential of the fluid in the pore, setting it equal to the chemical potential of the bulk fluid, and using an equation of state to determine the bulk density. Figure 13 contains this coexistence plot for the simulations and the two theories. The critical points for the simulations were determined approximately by extrapolating the T vs $\bar{\rho}$ plots.

The curves on this figure are monotonic and reveal little of the structure of the T vs $\bar{\rho}$ plots. The curves for the smaller radii are further away from the bulk coexistence curve and the critical points are at lower temperatures. This is true for LDA, the SDA, and the GCMC results. There are quantitative differences however, as reflected in Fig. 10. The predictions of the Kelvin equation are shown on each plot in Fig. 13. We used the bulk liquid properties appropriate to each theory and to the simulations to calculate these curves. The surface tensions for the simulated fluid are from previously published results[48] and from some recent ones.[49] The Kelvin equation, as in previous studies,[18,19] was found to overestimate the condensation pressure and the bulk density. In addition, the Kelvin equation includes no effect for the critical temperature decreasing below that of the bulk fluid.

In Fig. 14 we present the P, T diagram for the SDA and

Downloaded 09 Mar 2007 to 141.108.2.9. Redistribution subject to AIP license or copyright, see http://jcp.aip.org/jcp/copyright.jsp

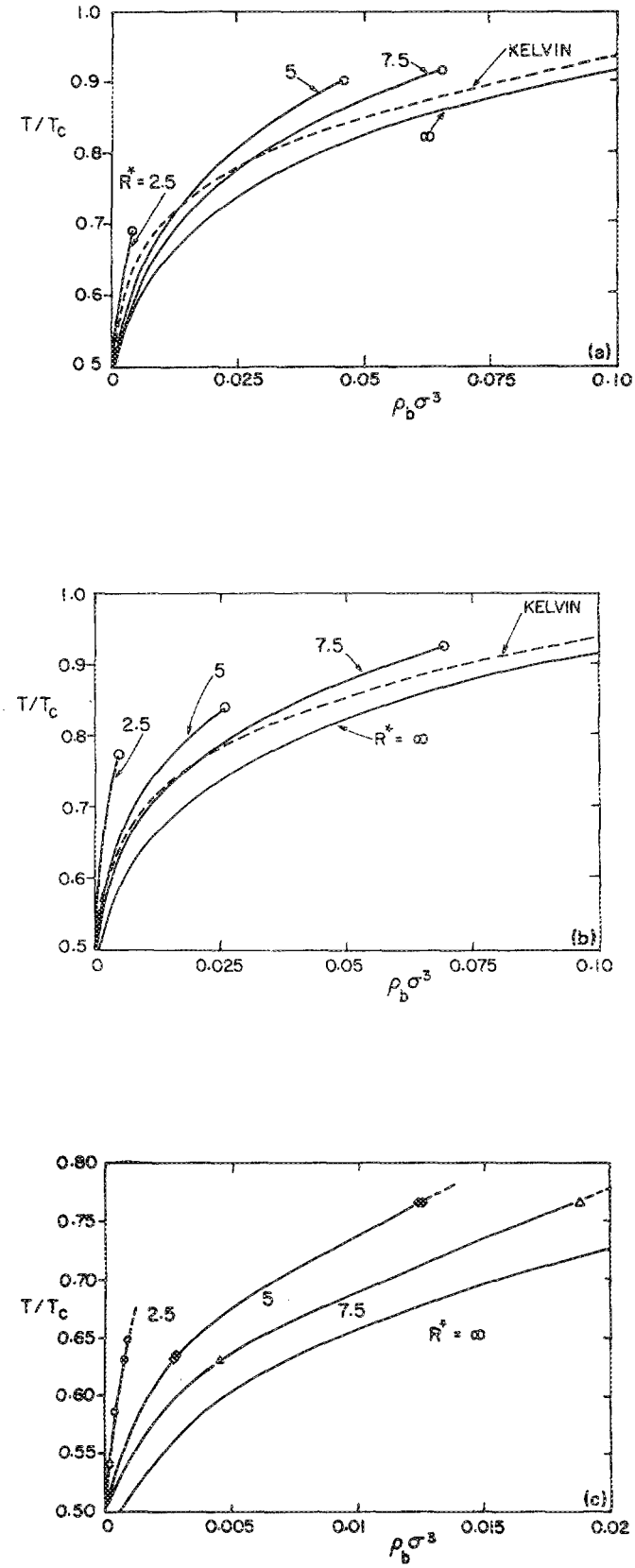

FIG. 13. Coexistence diagrams for the confined fluid. Relative temperature vs the bulk density. (a) LDA. The dashed curve shows the Kelvin prediction for $R^* = 2.5$. For the larger radii the Kelvin prediction is similar and lie between the dashed and the curve labeled by $R^* = \infty$. The capillary critical points are denoted by open circles. (b) SDA. Key as in (a). (c) Simulation results. Open symbols correspond to MD results. Filled symbols refer to GCMC. The exact critical points are unknown.

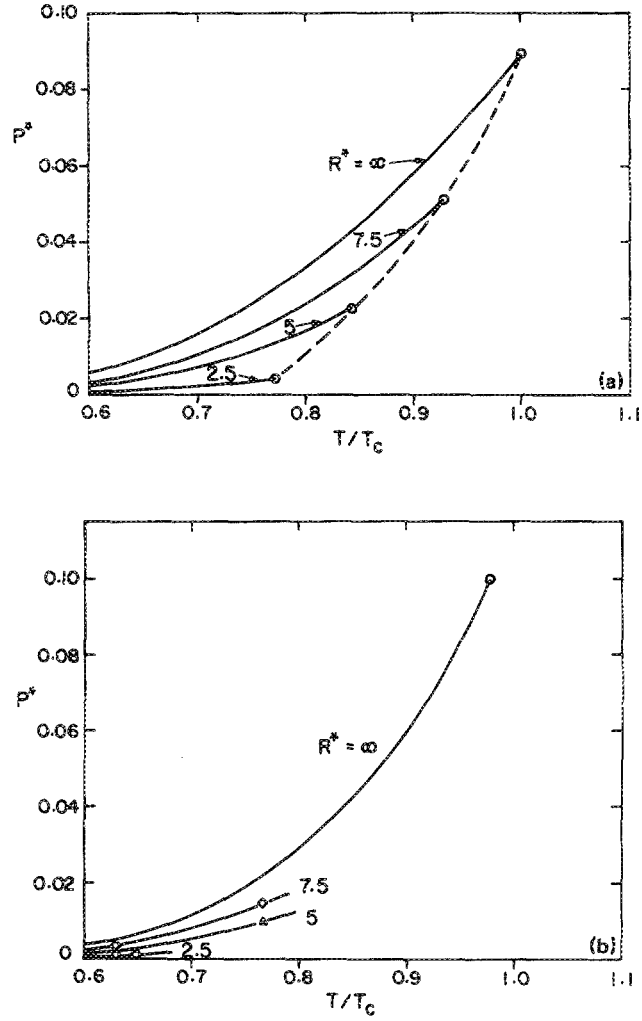

FIG. 14. Pressure–temperature phase diagram for the cut and shifted Lennard–Jones fluid confined to a cylindrical pore. The vapor pressure curve for the bulk fluid is labeled by $R^* = \infty$. (a) SDA results. The open circles denote the critical points and they have been linked by a dashed line. (b) Simulation results as obtained by MD. The critical points are unknown for the confined fluid.

the simulation. A similar diagram was published previously for the LDA results.[7] Figure 14 shows how the transition pressure at a fixed temperature decreases as the radius decreases. As shown in Fig. 13, the coexistence curve shortens as the radius is reduced, reflecting the reduction of the capillary critical temperature. The coexistence curves for different radii have similar shapes, but we note that plotting the pressure vs temperature in a reduced form (i.e., reducing by the values at the capillary critical point) does not result in a single curve.

V. CONCLUSIONS

We have presented extensive simulation results for adsorption isotherms both from GCMC and MD and located capillary condensation for a variety of radii and relative temperatures T/T_c. The simulation results have been compared with the local (LDA) and nonlocal (SDA) mean field density functional approximations. As expected,[19] the LDA gives only qualitative agreement with simulation for the ca-

Downloaded 09 Mar 2007 to 141.108.2.9. Redistribution subject to AIP license or copyright, see http://jcp.aip.org/jcp/copyright.jsp

pillary condensation pressure and fails to describe the fluid structure. In contrast the SDA appears a successful approach, providing good quantitative agreement for $R^* \geqslant 2.5$ with all the simulation results, transition pressure, order parameters and density profiles. We have shown that for larger radii ($R^* \gtrsim 5$) the coexistence phase diagram for the SDA and simulation (see Fig. 10) is changed considerably from the smooth dome shaped curves found with LDA. This is caused by a sudden increase in the adsorption close to the phase transition. This is reflected in the density profiles that show relatively sudden increases in the heights of the peaks near the wall.

ACKNOWLEDGMENTS

It is a pleasure to thank Pedro Tarazona for supplying us with a copy of a program that he developed in collaboration with one of us (UMBM). We also thank Steve Thompson for making surface tension data available prior to publication, and John Jackson for doing the photography. This work was supported by the Materials Science Center at Cornell, the Gas Research Institute, and the National Science Foundation (U.S./Spain Grant No. CCB-850-4023). Most of the computations presented in the work were performed at the Cornell National Supercomputer Facility which is supported, in part, by the National Science Foundation and the IBM Corporation.

APPENDIX

TABLE II. GCMC simulation data (see also Ref. 19).

μ'/ϵ[a]	$\bar{\rho}\sigma^3$[b]	NCONF[c]	P/P_{sat}[d]	$U_{tot}/N\epsilon$[e]
		$R^* = 1.0, T^* = 1.0$		
−10.195	0.00871	4	0.00061	−8.761
−9.195	0.0225	4	0.00166	−8.693
−8.695	0.0359	4	0.00274	−8.990
−8.195	0.0553	4	0.00452	−8.955
−7.695	0.0809	4	0.00746	−9.258
−7.195	0.113	4	0.0123	−9.422
−6.695	0.145	4	0.0215	−9.486
−6.195	0.172	4	0.0338	−9.542
−5.195	0.215	4	0.0929	−9.712
−4.695	0.230	4	0.1554	−9.759
−4.195	0.240	4	0.2638	−9.798
−3.695	0.249	4	0.4591	−9.798
−3.195	0.256	4	0.8568	−9.822
−2.695	0.262	4	···	−9.833
−2.195	0.266	4	···	−9.871
−1.695	0.271	4	···	−9.900
7.805	0.280	4	···	−9.450
		$R^* = 1.0, T^* = 0.2$		
−10.7220	0.000148	4		−9.798
−10.122	0.00480	4		−9.887
−10.072	0.00700	4		−9.819
−10.022	0.0106	4		−9.997
−9.972	0.0183	4		−10.221
−9.972	0.0181	4		−10.037
−9.922	0.0374	4		−10.220
−9.872	0.0726	4		−10.397
−9.822	0.1467	4		···
−9.772	0.2104	4		−10.627
−9.672	0.2581	4		−10.709
−9.422	0.2734	4		−10.755
−9.172	0.2779	4		−10.777

TABLE II. (*continued*).

μ'/ϵ[a]	$\bar{\rho}\sigma^3$[b]	NCONF[c]	P/P_{sat}[d]	$U_{tot}/N\epsilon$[e]
−8.922	0.2797	4		−10.786
−8.422	0.2801	4		−10.787
−7.922	0.2801	4		−10.781
		$R^* = 5.0, T^* = 0.85$		
−7.573	0.00076	9	0.005310	−2.45
−6.573	0.00252	9	0.01705	−2.47
−5.573	0.00865	9	0.05927	−2.46
−4.573	0.03527	9	0.1873	−2.760
−4.473	0.04190	9	0.2123	−2.818
−4.373	0.05024	9	0.2402	−2.878
−4.273	0.06120	9	0.2719	−2.912
−4.173	0.07603	9	0.3083	−3.073
−4.073	0.09750	9	0.3498	−3.023
−3.973	0.1332	9	0.3974	−3.414
−3.883	0.2193	3	0.4470	−3.99
−3.873	0.2191	9	0.4528	−3.823
−3.873	0.5116	3	0.4528	−4.77
−3.797	0.5272	5	0.5008	−4.858
−3.773	0.5311	3	0.5170	−4.880
−3.073	0.5987	3	0.6590	−5.036
−2.573	0.6296	3	···	−5.486
−2.150	0.6472	3	···	−5.59
		$R^* = 7.5, T^* = 0.85$		
−5.573	0.0056	1.5		−2.116
−5.073	0.0106	1.5		−2.173
−4.573	0.0215	1		−2.308
−4.373	0.0296	1		−2.400
−4.173	0.0420	1		−2.530
−3.973	0.0663	1		−2.772
−3.873	0.0834	1		−2.917
−3.773	0.1260	1		−3.250
−3.673	0.2280	1		−3.797
−3.673	0.5570	1		−4.490
−3.623	0.3060	1		−4.050
−3.573	0.5850	1		−4.650
−3.573	0.3710	1		−4.237
−3.523	0.5900	1.9		−4.680
−3.473	0.5910	1		−4.689
−3.373	0.6112	1.5		−4.809
−3.173	0.6260	1.5		−4.898
−2.973	0.6471	1.5		−5.031

[a] Configurational chemical potential as defined in Eq. (23).
[b] Average number of particles in the pore as defined in Eq. (29).
[c] Number (in millions) of configurations after equilibration.
[d] Bulk pressure reduced by the bulk saturation pressure.
[e] Total potential energy per particle.

[1] R. Evans and P. Tarazona, Phys. Rev. Lett. **52**, 557 (1984).
[2] R. Evans and U. Marini Bettolo Marconi, Chem. Phys. Lett. **114**, 415 (1985).
[3] R. Evans and U. Marini Bettolo Marconi, Phys. Rev. A **32**, 3817 (1985).
[4] B. K. Peterson, J. P. R. B. Walton, and K. E. Gubbins, Int. J. Thermophys. **6**, 585 (1985).
[5] R. Evans, U. Marini Bettolo Marconi, and P. Tarazona, J. Chem. Phys. **84**, 2376 (1986).
[6] R. Evans, U. Marini Bettolo Marconi, and P. Tarazona, J. Chem. Soc. Faraday Trans. 2 **82**, 2376 (1986).
[7] B. K. Peterson, J. P. R. B. Walton, and K. E. Gubbins, J. Chem. Soc. Faraday Trans. 2 **82**, 1789 (1986).
[8] B. K. Peterson, J. P. R. B. Walton, and K. E. Gubbins, *Proceedings of the 2nd International Conference on Fundamentals of Adsorption*, edited by A. I. Liapis (Engineering Foundation, New York, 1987), p. 463.
[9] P. Tarazona, U. Marini Bettolo Marconi, and R. Evans, Mol. Phys. **60**, 573 (1987).
[10] R. Evans and U. Marini Bettolo Marconi, J. Chem. Phys. **86**, 7138 (1987).
[11] U. Heinbuch and J. Fischer, Ref. 8, p. 245.

Downloaded 09 Mar 2007 to 141.108.2.9. Redistribution subject to AIP license or copyright, see http://jcp.aip.org/jcp/copyright.jsp

[12]U. Heinbuch and J. Fischer, Chem. Phys. Lett. **135**, 587 (1987).
[13]U. Heinbuch and J. Fischer, Mol. Simul. **1**, 109 (1987).
[14]J. E. Lane and T. H. Spurling, Aust. J. Chem. **33**, 231 (1980).
[15]W. Van Megen and I. K. Snook, Mol. Phys. **54**, 741 (1985).
[16]J. J. Magda, M. Tirrell, and H. T. Davis, J. Chem. Phys. **83**, 1888 (1985); **84**, 2901 (1986).
[17]J. P. R. B. Walton and N. Quirke, Chem. Phys. Lett. **129**, 382 (1986).
[18]G. S. Heffelfinger, F. Van Swol, and K. E. Gubbins, Mol. Phys. **61**, 1381 (1987).
[19]B. K. Peterson and K. E. Gubbins, Mol. Phys. **62**, 215 (1987).
[20]E. M. Piotrovskaya and N. A. Smirnova (preprint).
[21]M. Schoen, D. J. Diestler, and J. H. Cushman, J. Chem. Phys. **87**, 5464 (1987).
[22]A. Z. Panagiotopoulos, Mol. Phys. **62**, 701 (1987).
[23]J. G. Powles, G. Rickayzen, and M. L. Williams (preprint).
[24]P. Tarazona, Phys. Rev. A **31**, 2672 (1985); see also **32**, 3148 (1985).
[25]T. F. Meister and D. M. Kroll, Phys. Rev. A **31**, 4055 (1985).
[26]W. A. Curtin and N. W. Ashcroft, Phys. Rev. A **32**, 2909 (1985).
[27]R. Evans, Adv. Phys. **28**, 143 (1979).
[28]D. E. Sullivan, Phys. Rev. B **20**, 3991 (1979).
[29]J. D. Weeks, D. Chandler, and H. C. Andersen, J. Chem. Phys. **54**, 5237 (1971).
[30]B. Q. Lu, R. Evans, and M. M. Telo da Gama, Mol. Phys. **55**, 1319 (1985).
[31]D. E. Sullivan and M. M. Telo da Gama, *Fluid Interfacial Phenomena*, edited by C. A. Croxton (Wiley, New York, 1986), p. 45.
[32]J. Fischer, U. Heinbuch, and M. Wendland, Mol. Phys. **61**, 953 (1987).
[33]P. Ball and R. Evans, Mol. Phys. **63**, 159 (1988).
[34]B. Widom, J. Chem. Phys. **39**, 2808 (1963).
[35]J. S. Rowlinson and B. Widom, *Molecular Theory of Capillarity* (Oxford University, New York, 1982).
[36]M. Bishop, Am. J. Phys. **52**, 158 (1984).
[37]Z. W. Salsburg, J. G. Kirkwood, and R. W. Zwanzig, J. Chem. Phys. **21**, 1098 (1953).
[38]Lord Rayleigh, Nature **45**, 80 (1891).
[39]L. Tonks, Phys. Rev. **50**, 955 (1936).
[40]F. Van Swol (unpublished results).
[41]M. Toda, R. Kubo, and N. Saitô, *Statistical Physics I* (Springer, Berlin, 1983).
[42]L. Verlet, Phys. Rev. **159**, 98 (1967).
[43]D. Brown and J. H. R. Clarke, Mol. Phys. **51**, 1243 (1984).
[44]D. J. Adams, Mol. Phys. **29**, 307 (1975).
[45]E. Bruno, U. Marini Bettolo Marconi, and R. Evans, Physica A **141**, 187, (1987).
[46]J. S. Rowlinson, Proc. R. Soc. London Ser. A **402**, 67 (1985).
[47]J. Chalupa and B. A. Huberman, J. Chem. Phys. **72**, 5276 (1980).
[48]G. A. Chapela, G. Saville, J. S. Rowlinson, and S. M. Thompson, Chem. Soc. Faraday Trans. 2 **73**, 1133 (1977).
[49]S. M. Thompson (unpublished results).
[50]J. H. Sikkenk, J. O. Indekeu, J. M. J. Van Leeuwen, and E. O. Vossnack, Phys. Rev. Lett. **59**, 98 (1987).
[51]J. F. Knight and P. A. Monson, J. Chem. Phys. **84**, 1909 (1986).

Downloaded 09 Mar 2007 to 141.108.2.9. Redistribution subject to AIP license or copyright, see http://jcp.aip.org/jcp/copyright.jsp